Space group analysis of $Sr_{1-x}Ca_xTiO_3$ ceramics with x = 0.20, 0.27 and 0.30 through electron diffraction

2007 J. Phys.: Condens. Matter 19 436210

(http://iopscience.iop.org/0953-8984/19/43/436210)

IOP PUBLISHING JOURNAL OF PHYSICS: CONDENSED MATTER

J. Phys.: Condens. Matter **19** (2007) 436210 (19pp) doi:10.1088/0953-8984/19/43/436210

Space group analysis of $Sr_{1-x}Ca_xTiO_3$ ceramics with $x = 0.20$, 0.27 and 0.30 through electron diffraction

Shahid Anwar and N P Lalla

UGC-DAE Consortium for Scientific Research, University Campus, Khandwa road, Indore 452001, India

E-mail: nplalla@csr.ernet.in

Received 29 May 2007, in final form 5 September 2007
Published 26 September 2007
Online at stacks.iop.org/JPhysCM/19/436210

Abstract

The space groups of $Sr_{1-x}Ca_xTiO_3$ in the composition range $0.20 \leqslant x \leqslant 0.30$ have been investigated using powder x-ray diffraction (XRD) and electron diffraction techniques. Electron diffraction has been used in selected area diffraction (SAD), convergent beam electron diffraction (CBED) and micro-diffraction modes to record zero-order Laue zone (ZOLZ) and higher-order Laue zone (HOLZ) patterns. For the $0.20 \leqslant x \leqslant 0.30$ composition range there is still controversy regarding the correct space group: $P2_1/m$, $Pnma$, $Imma$ or $I4/mcm$. By invoking Rietveld refinement, detailed analysis of CBED patterns containing A_2-type GM-lines and comparison between simulated ZOLZ/FOLZ and experimentally observed SAD patterns, we have established that for $Sr_{1-x}Ca_xTiO_3$ ($0.20 \leqslant x \leqslant 0.30$) two types of phase coexist at room temperature. These are the $Pnma$ and $P2_12_12$ orthorhombic phases, coexisting with volume fractions of about 40% and 60% respectively.

1. Introduction

Phase transition studies in ABO_3 perovskite compounds have received wide attention from the scientific as well as the technological point of view (Jaffe *et al* 1971). Strontium titanate ($SrTiO_3$) is an ideal system to study structural phase transitions and critical phenomena. It undergoes an antiferro–distortive phase transition due to the softening of a zone boundary phonon modes around 105 K (Mitsui and Westphal 1961, Cowley 1980). Introducing polar ordering by substitution of Ca^{+2}, Ba^{+2}, Pb^{+2} (Bernorz and Muller 1984) in $SrTiO_3$ or by the application of external stress (Uwe and Sakudo 1976) and electric field (Hembergger *et al* 1995), a number of phase transitions have been observed. Crystal structures across the perovskite system $Sr_{1-x}Ca_xTiO_3$ (SCT) have been the subject of a number of studies but the results are still in dispute. It is well know that the $CaTiO_3$ and $SrTiO_3$ systems are completely miscible. Starting with a lower Ca content in $Sr_{1-x}Ca_xTiO_3$ than in $CaTiO_3$, SCT exhibits a variety of structural phases. The room-temperature structure of $SrTiO_3$ is cubic, with space

group $Pm3m$, and that of $CaTiO_3$ is orthorhombic, with space group $Pbnm$ (or $Pnma$). In the mixed $Sr_{1-x}Ca_xTiO_3$ system, above a certain level of Ca concentration, the structure changes from cubic to orthorhombic. There are several controversies about the room-temperature structure of SCT as a function of Ca content.

Previously, Granicher and Jakits (1954), based on low-resolution XRD data, proposed that the room-temperature structure of SCT is nearly cubic. Ball *et al* (1998), based on synchrotron x-ray diffraction studies, and Qin *et al* (2000), by laboratory XRD, determined the unit cell parameters, and from the splitting of perovskite peaks concluded that the structure is tetragonal with space group $I4/mcm$ for $0.1 \leqslant x \leqslant 0.35$, orthorhombic ($Cmcm$) for $0.40 \leqslant x \leqslant 0.55$, and $Pnma$ above $x > 0.55$. Ceh *et al* (1987) proposed a cubic to orthorhombic phase boundary at $x = 0.40$. A different sequence of structures is proposed by Ranjan and Pandey (2001a, 2001b), claiming that the structure is not tetragonal, but orthorhombic in the composition range $0.12 \leqslant x \leqslant 0.40$. The earlier-proposed $Pnma$ structure was later reanalyzed to be $Imma$, based on improved data quality (Mishra *et al* 2002). The assignment to $Imma$ is based largely on the Rietveld refinement of laboratory XRD and neutron scattering data only. This is supported by observing the asymmetry of the Eg lines and broad bands in the Raman spectra (Ranson *et al* 2005). There are very few reports on electron diffraction on SCT in the composition range discussed here. Ranjan *et al* (2001), using electron diffraction, showed that the structure is cubic for $x < 0.06$, orthorhombic with different symmetry in the composition range $0.09 < x \leqslant 1.0$, and for $0.06 < x < 0.09$ is either tetragonal or orthorhombic, but definitely not cubic. However, in recent reports, Howard *et al* (2001, 2005) and Carpenter *et al* (2006) assigned a tetragonal structure with space group $I4/mcm$ for the SCT30 at room temperature, whereas Woodward *et al* (2006), based on electron diffraction studies, report a $P2_1/m$ structure for SCT30. In fact they have given a new sequence of structural transitions in the SCT phase diagram. According to them the space groups are $Pm3m$ for $x = 0$, $I4/mcm$ for $x < 0.2$, $C2/m$ for $x = 0.2$, $P2_1/m$ for $0.2 < x < 0.6$ and $Pnma$ for $x > 0.6$.

In certain cases, like SCT, identifying the correct space group using x-ray or neutron diffraction is difficult, due to the considerably weak x-ray scattering factor for oxygen ions. Because of this weak scattering factor the information concerning the oxygen sublattice gets diluted. Structural distortions give rise to some new peaks with weak intensities, which appear as splitting in the existing peaks. Proper identification of such peaks is decisive for the space group identification, but due to limited resolution, the peak splitting may not be seen. Neutron diffraction can solve the problem of the weak contribution from the oxygen sublattice, but usually, due to low incident flux, the problem of resolution persists, even for neutron scattering too. Electron diffraction has the advantage that single-domain diffraction patterns can routinely be obtained from relatively smaller regions of $\sim$0.1 μm, and since electrons interact with the oxygen sublattice much more strongly than x-rays, it allows observation of even the weakest superlattice peaks. Unlike powder x-ray and neutron scattering data, which are one-dimensional (1D) projections of three-dimensional (3D) structural information, electron diffraction provides two-dimensional (2D) and 3D information of the structure. The problem of determination of correct space group/symmetry elements, which emanates mainly from the resolution-limited observation in the x-ray and neutron techniques, is relatively easily solved by the occurrence of symmetry features and other characteristic features, like GM-lines, present in the electron diffraction patterns. Convergent beam electron diffraction (CBED), combined with zone-axis micro-diffraction including ZOLZ and FOLZ patterns, provides information of the crystal lattice type together with its symmetry.

Thus keeping in view the above-mentioned controversies regarding the room-temperature space group of SCT with $0.20 \leqslant x \leqslant 0.30$, we have carried out a detailed study using XRD and transmission electron microscopy (TEM), to probe the room-temperature space group of SCT

in the above composition range. We have used symmetry analysis of CBED patterns, including features like GM-lines, and have finalized the presence of the *Pnma* phase. The presence of a new orthorhombic phase with space group $P2_12_12$ coexisting with the *Pnma* phase has also been identified.

2. Experimental details

Single-phase $Sr_{1-x}Ca_xTiO_3$ ceramics with $x = 0.20$, 0.27 and 0.30, hereafter expressed as SCT20, SCT27 and SCT30, were prepared following the conventional solid-state reaction technique. High-purity (99.99%) powders of $SrCO_3$, $CaCO_3$ and TiO_2 were preheated at 150 °C to remove the adsorbed moisture and then weighed according to the above stoichiometric proportions and wet-mixed using acetone as the mixing medium. The mixed and dried powder was calcined in air at 1100 °C for 6 h, followed by multiple grinding and calcinations at 1250 °C. The final calcined powder was uniaxially pelletized at 100 kN cm^{-2} pressure into 15 mm diameter × 1 mm thick pellets using polyvinyl alcohol as binder. The pellets were then sintered at 1300 °C for 12 h. It should be noted that the earlier workers (Ranjan and Pandey 2001b) have sintered the pellets at 1300 °C for 6 h only. The sintered pellets were gently crushed to fine powder and subsequently annealed at 600 °C for ∼10 h to remove the residual strain produced during grinding of the final sintered pellets. Since the aim of the present work is to carry out detailed space group characterization of the prepared SCT materials, which have already been studied quite extensively, it became quite necessary for us to prepare high-quality samples that have achieved an equilibrium state. Therefore, after each heat treatment the full-width at half-maximum (FWHM) of a high-angle peak at ∼86.7° was monitored. For the initial calcined powders, the FWHM was found to be >0.3°, whereas for the final sintered ceramics the FWHM was reduced to 0.12°. The occurrence of such a sharp peak indicates the equilibrium state of the sample. Another test of the high quality of our samples can be confirmed through the comparison (Ranjan *et al* 2000, Ranjan and Pandey 2001b) of dielectric measurement results, as described below. Only the final heat-treated powder was used for the diffraction studies, as described below.

The as-prepared powder samples of SCT20, SCT27 and SCT30 were subjected to detailed structural and phase purity characterizations using powder x-ray diffraction (XRD). The XRD was carried out using Cu Kα x-rays on a Rigaku diffractometer working in Bragg–Brentano para-focusing geometry and mounted on a rotating-anode x-ray generator operating at 15 kW output power. Back-scattered electron imaging using a JEOL-SEM 5600 scanning electron microscope was also carried out for all the above-mentioned samples to explore the possibilities of any impurity phase whose signature might have been masked under the background of the bulk XRD data. The compositions of Sr, Ca and Ti of the synthesized samples were verified using an energy-dispersive analysis of x-rays (EDAX). The complete absence of any contrast variation, appearing due to different effective-Z for different phases, in the back-scattered SEM micrograph confirmed the phase purity of these samples. EDAX revealed that the concentrations of Sr, Ca and Ti were the same as that of the starting compositions within the typical EDAX error.

Transmission electron microscopy (TEM) was carried out employing a Tecnai G^220 transmission electron microscope (FEI) operating at 200 kV and equipped with LaB_6 filament and a charge-coupled device (CCD) camera (Mega view SIS). Samples for TEM observation were made by dispersing the powders in methanol and drying a drop of the dispersion on a perforated carbon-coated copper grid. TEM was performed in imaging, SAD, micro-diffraction and CBED modes.

For TEM analysis, a double-tilt holder with tilt capabilities $\alpha = \pm 45°$ and $\beta = \pm 25°$ was used. Whenever they were required, the SAD patterns were obtained by tilting the required

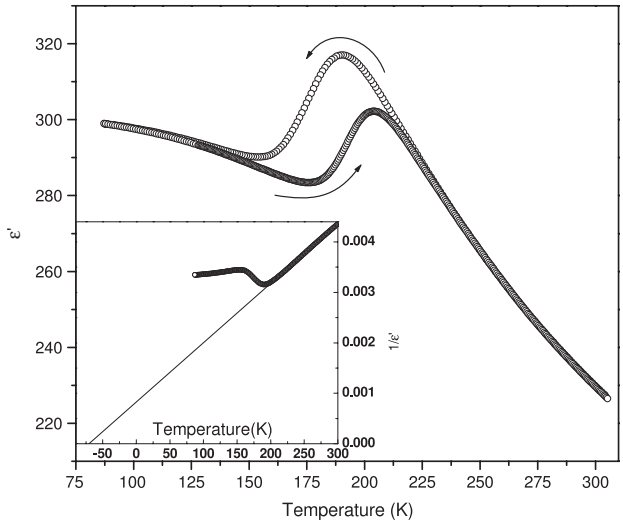

Figure 1. Temperature-dependent dielectric measurement of $Sr_{0.7}Ca_{0.3}TiO_3$ at 10 kHz, exhibiting the occurrence of an antiferroelectric phase transition. The inset shows a Curie–Weiss plot.

zone exactly along the beam direction. This was done partially by double-tilt action of the holder and finally using the beam-tilt capability of the dark-field mode. The micro-diffraction and CBED patterns were obtained using a 10 μm condenser aperture with the incident electron beam converging to an effective spot-size of 50 nm on the specimen. The small spot-size assures good spatial resolution and minimizes the likelihood of any significant thickness and orientation variations within the diffracting specimen volume. All the TEM photographs, particularly the SAD, micro-diffraction and CBED patterns which have been presented here, are properly enhanced for the clear visibility of even the weakest details like weak superlattice spots, HOLZ rings and GM-lines. In general in pristine diffraction patterns, these features may remain undetected otherwise. During TEM analysis, EDAX was also carried out. The observed compositions were found to match the intended ones within the typical EDAX error.

3. Results and discussions

3.1. Dielectric studies

Figure 1 shows the temperature-dependent permittivity data of $Sr_{0.7}Ca_{0.3}TiO_3$ ceramics at 10 kHz. The inset shows the plot of the inverse of permittivity versus temperature and its fit with Curie–Weiss behavior. The observed negative value of the Curie–Weiss temperature ($T_c \sim -75$ K) confirms the occurrence of antiferroelectric phase transition, as reported (Ranjan *et al* 2000). The nature of the observed phase transformation, the estimated value of the Curie temperature T_c and the room-temperature permittivity value of our sample match quite well with those of the available literature (Ranjan *et al* 2000, Ranjan and Pandey 2001b). This confirms the high quality and the equilibrium state of the prepared SCT ceramic samples used for the structural studies in the present case.

3.2. X-ray diffraction studies

Figure 2 depicts representative Rietveld refined x-ray diffraction patterns of SCT30 corresponding to different space groups. Since all the three compositions which have been studied here depict the same features, we have presented here only a representative one,

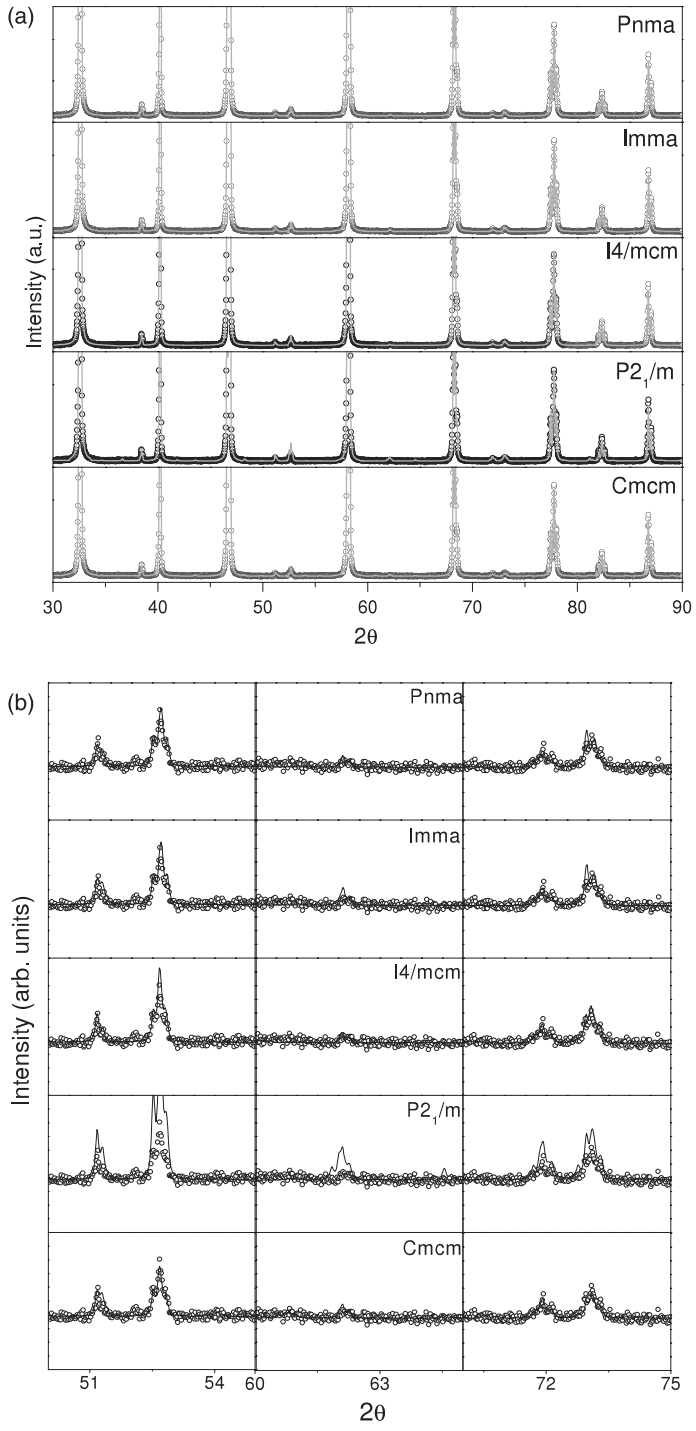

Figure 2. (a) Rietveld refined x-ray diffraction patterns of $Sr_{0.7}Ca_{0.3}TiO_3$, using space group $Pnma$, $Imma$, $I4/mcm$, $P2_1/m$ and $Cmcm$. (b) Expanded view of some of the superlattice peaks taken from the diffraction pattern shown in (a). The fit corresponding to $P2_1/m$ is not good.

i.e. SCT30. The same fitting strategy was followed for each space group case. The five space groups under consideration differ only in the style of rigid rotation of the BO_6 octahedral unit with respect to its most symmetric orientation in the basic perovskite structure with $Pm3m$ space group. Therefore the fitting strategies differed only in the choice of extra Wyckoff positions and switching on and off their relaxation as permitted by the space group considered. The absence of any unaccounted for peak in the XRD profile from any of the space group fittings confirms the phase purity of the sample. Enlarged views of a few selected regions of the fitted patterns having superlattice peaks have also been shown so that the fit qualities corresponding to different space groups can be vividly judged. However, it was not possible to select the correct space group on the basis of Rietveld refinement, since out of the five, $Pnma$, $Imma$, $Cmcm$ and $I4/mcm$ gave comparable χ^2 values. But of course the fit based on $P2_1/m$ did not give a good qualitative fit for even the basic perovskite peaks. The enlarged views corresponding to $P2_1/m$ clearly show that the superlattice peaks are not properly fitted. This tells us that the space group is definitely not $P2_1/m$. The fit qualities corresponding to the remaining four possibilities, $Imma$, $I4/mcm$, $Cmcm$ and $Pnma$, are equally good, and hence based entirely on the comparison of the fit and the χ^2 values, it was not possible to distinguish the unique one.

The two possible orthorhombic systems, with space groups $Imma$ and $Pnma$, have a similar pseudo-tetragonal lattice and differ only by an in-phase tilt. $Imma$ results from an $a^-a^-c^0$ tilt system and $Pnma$ from an $a^-a^-c^+$ tilt system, as described in Glazer tilt notations (Glazer 1972, 1975). It has been argued by Ranjan and Pandey (2001b), Ranjan *et al* (2005) that under the assumption of rigid octahedra tilt the intensity of ooe (odd–odd–even) type reflections would be zero. In principle the diffraction patterns from these systems can be differentiated. But in x-ray/neutron diffraction patterns the peak intensity, which comes from the in-phase tilt is too weak to be detected above the background. Hence it is difficult to distinguish between the tilts $a^-a^-c^0$ and $a^-a^-c^+$ with x-ray/neutron diffraction. Because of the above subtleties related to space group determination, a detailed electron diffraction study was carried out.

3.3. Electron diffraction studies

Before we proceed to describe and discuss our results of electron diffraction studies it is necessary to discuss the approach followed by some of the workers in this area. Ranjan *et al* (2002) have produced micro-diffraction patterns corresponding to all the three mutually orthogonal axes [100], [010], and [001]. Practically, it is not possible to obtain all three from the same grain, due to mechanical limitations of the β-tilt of a double-tilt holder. In fact even getting two mutually perpendicular zones from a single grain demands being fortunate enough to encounter a grain lying in a favorable orientation. Thus practically in most cases different zone patterns are obtained only from different grains. Because of this there may be chance of mixing of patterns from different phases, and hence misinterpretation of the space group. Woodward *et al* (2006) have given a method in which one needs to collect patterns from different grains and the decision is based on the statistics of observing zone patterns with a certain type of reflections. Howard *et al* (2005) in their recent reports based on analysis of SAD patterns have assigned the $I4/mcm$ space group to SCT30. However, after digital enhancement well-defined superlattice reflections were observed, which are neither expected in a body-centered lattice nor will appear as double diffraction.

Therefore in the present study we have followed the conventional way of space group determination (Williams and Carter 1996, Morniroli and Steeds 1992). For this we have recorded SAD, CBED and micro-diffraction patterns from the same region of a single domain. By comparison with the simulated patterns, we have discarded the possibility of some of the expected space groups. We have not tried to compare the intensities of the reflections. Our

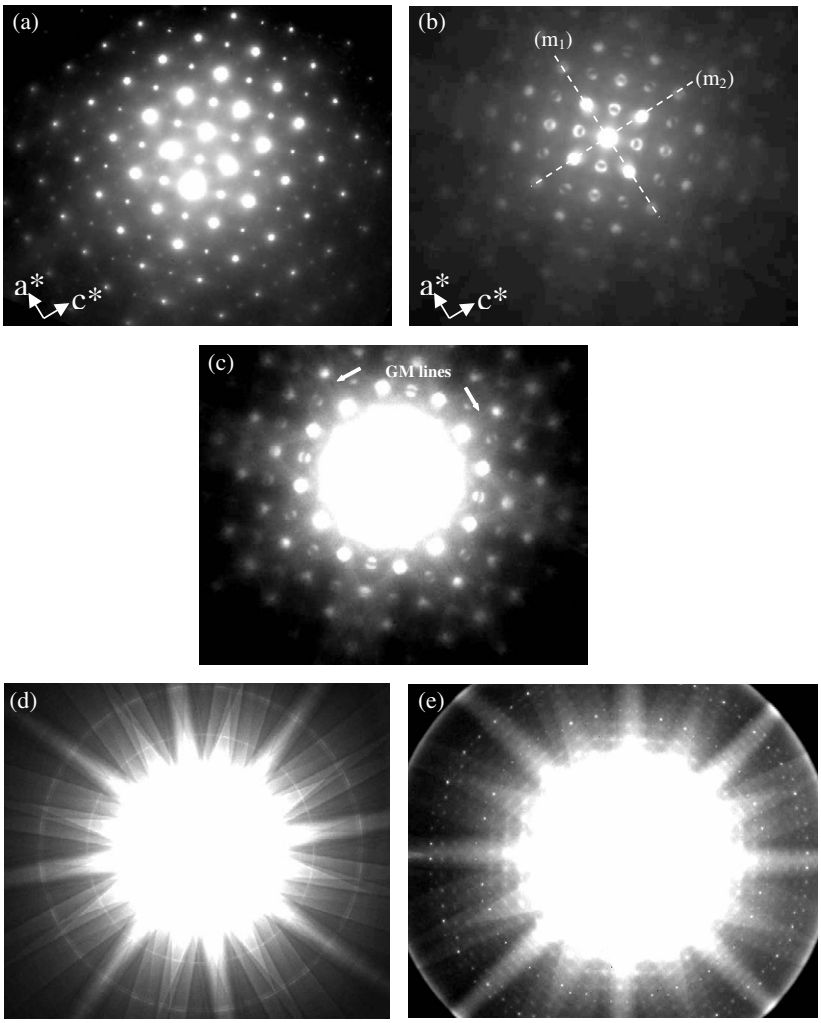

Figure 3. (a) Selected area electron diffraction (b) and (c) convergent beam electron diffraction (CBED), (d) wide-angle CBED, and (e) focused micro-diffraction pattern from SCT30 along the [010] zone of the *Pnma* space group. The CBED pattern on (c) has been enhanced to make clear the presence of GM-lines, as indicated by arrows. The dotted lines represent the mirrors along a^* and c^* representing 2*mm* dark-field symmetry.

decisions are purely based on the absence or presence of certain reflections and diffraction features like GM-lines in an otherwise properly processed diffraction pattern. For enhancement of the patterns, brightness and contrast were varied using linear or logarithmic functions. This was done using the Analysis software made available with the CCD camera. The decisions regarding the correct space group have been taken based on the systematic absence of reflections and presence of proper signatures of symmetry elements as indicated by the presence of GM-lines (Tanaka 1989, Williams and Carter 1996) appearing in kinematically forbidden reflections in a CBED pattern.

Figure 3(a) shows the SAD pattern taken along a zone axis, which at first glance may be considered either the [010] zone of the $Pnma$, $P2_1/m$ and $Imma$, or [001] zone of $I4/mcm$ and $Cmcm$. This pattern was recorded by tilting the zone axis exactly along the beam direction.

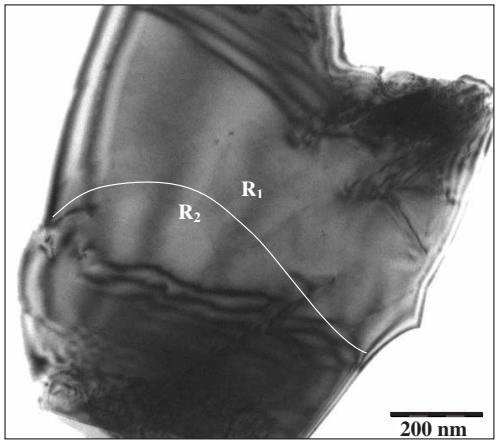

Figure 4. Bright-field electron micrograph of an electron-transparent particle of size about 1 μm. The two regions R_1 and R_2 were found to be structurally different.

Tilting the zone axis along the exact beam direction was accomplished in two steps. First this was tilted very close to the zone axis by double-tilt action of the holder being in the SAD mode. The final alignment was achieved after switching to CBED mode and then obtaining the best possible symmetric CBED pattern from the same area of the sample, using the beam-tilt facility of the dark-field mode. Once the exact zone alignment was achieved in the area of interest, we switched back to the SAD mode and recorded the zone-axis pattern, an example of which is shown in figure 3(a). A CBED pattern so obtained is also shown in figure 3(b). Figure 3(c) shows the same CBED pattern as in figure 3(b) but with different brightness and contrast settings so as to make the presence of very weak A_2-type GM-lines clear in the kinematically forbidden reflections (003) and (300). These reflections are indicated by arrows. The GM-lines appear as a result of dynamical extinctions along the line of the exact Bragg condition in a kinematically forbidden reflection (Gjønnes and Moodie 1965, Williams and Carter 1996, Tanaka 1989). Figures 3(d) and (e) show wide-angle CBED and focused micro-diffraction patterns taken from exactly the same area as that of figure 3(b). The presence of two HOLZ rings in both the patterns can be seen.

During TEM exploration we invariably encountered two different types of region in the same single-crystal grain; see figure 4. In figure 4, the curved line roughly represents the boundary between the two regions denoted R_1 and R_2. It is remarkable that the two regions have almost no contrast difference in the bright-field image. The other region (R_2) was found to show a nearly similar SAD pattern as that of figure 3(a); see figure 5(a). The structural difference between the regions R_1 and R_2 became obvious only in low-angle and wide-angle CBED patterns taken from them. The diffraction patterns shown in figure 3 are obtained from R_1. The low-angle and wide-angle CBED patterns obtained from region R_2 are shown respectively in figures 5(b) and (c). The presence of A_2-type GM-lines (Gjønnes and Moodie 1965), indicated by arrows, can be clearly seen. Almost no clear presence of any FOLZ ring in the wide-angle CBED, taken along the exact zone, is seen in figure 5(c). This is quite contrasting when compared to figure 3(d). The presence of an FOLZ ring corresponding to the zone shown in figure 5(c) was realized only when the pattern was recorded in a considerably tilted orientation and the intensity of a part of the FOLZ ring was enhanced due to decreased effective scattering vector; see figure 5(d). This may be due to presence of disorder in the sample, and also due to weak intensity of the FOLZ layer, which contains only reciprocal lattice

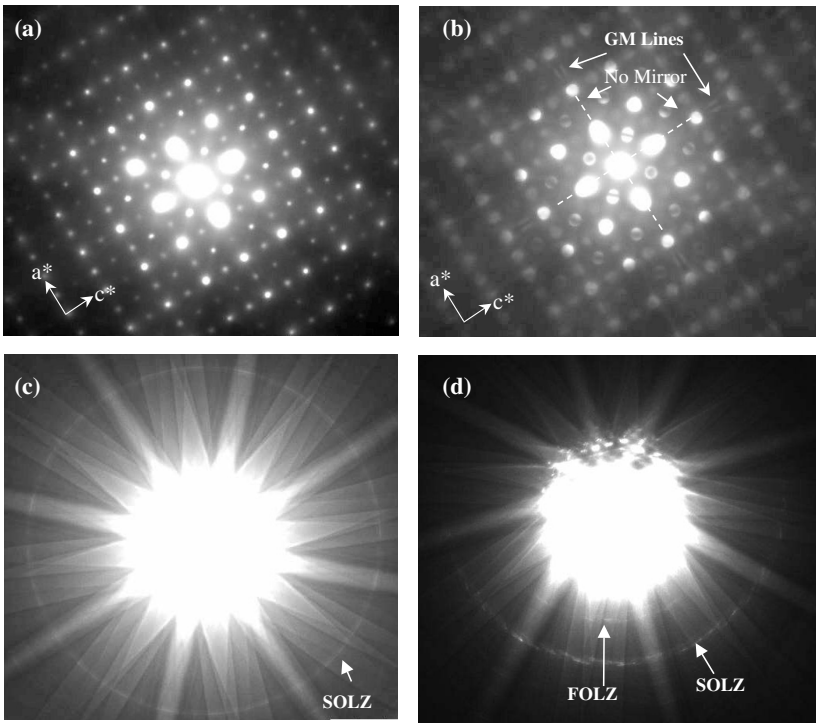

Figure 5. (a) Zone-axis selected area electron diffraction, (b) convergent beam electron diffraction (CBED), and (c), (d) wide-angle CBED patterns from region R_2 of SCT30. The presence of mutually perpendicular GM-lines has been indicated by arrows. The absence of mirrors unlike in figure 3(b) can be seen along the dotted lines. The presence of a weak FOLZ ring in the tilted CBED pattern has been indicated.

points, which appear as superlattice formation. The intensities of these superlattice peaks are always weak. During TEM observation we realized that in aggregate the volume fraction of R_1-like regions, i.e. those showing clear FOLZ rings, as shown in figures 3(d) and (e), is less compared to that of the R_2 regions. The typical thickness of any such grains giving these SAD patterns was measured, employing the contamination cap growth technique, to be ∼50 nm. The sets of SAD and low-angle and wide-angle CBED patterns corresponding to SCT20 and SCT27, exhibiting features identical to those shown in figure 3 for SCT30, are presented in figures 6(a)–(c) and (d)–(f) respectively and those identical to those shown in figure 5 for SCT30, are presented in figures 7(a)–(c) and (d)–(f) respectively. The insets in figures 7(b) and (e) are the unmodified central part of the corresponding patterns. The intensity distributions in these disks appear to be characteristics of the particular phase.

Figure 8(a) shows the SAD pattern taken from the same grain as shown in figure 4 after a proper tilt with respect to the zone-axis patterns shown in figures 3(a) and 5(a). The angle between the two was measured to be 45°. Figures 8(b) and (c) are the wide-angle CBED and micro-diffraction patterns taken from the same region. The presence of intense HOLZ rings can be seen in figures 8(b) and (c). After proper measurement of the reciprocal vectors and its angular separation of 45° with respect to the [010] zone, the SAD pattern in figure 8(a) was assigned to a [111]-type zone. This observation is true for any of the above-mentioned space groups. The HOLZ rings recorded in figures 8(b) and (c) correspond to SOLZ. We could not see any FOLZ even in a pattern recorded in a considerably tilted setting.

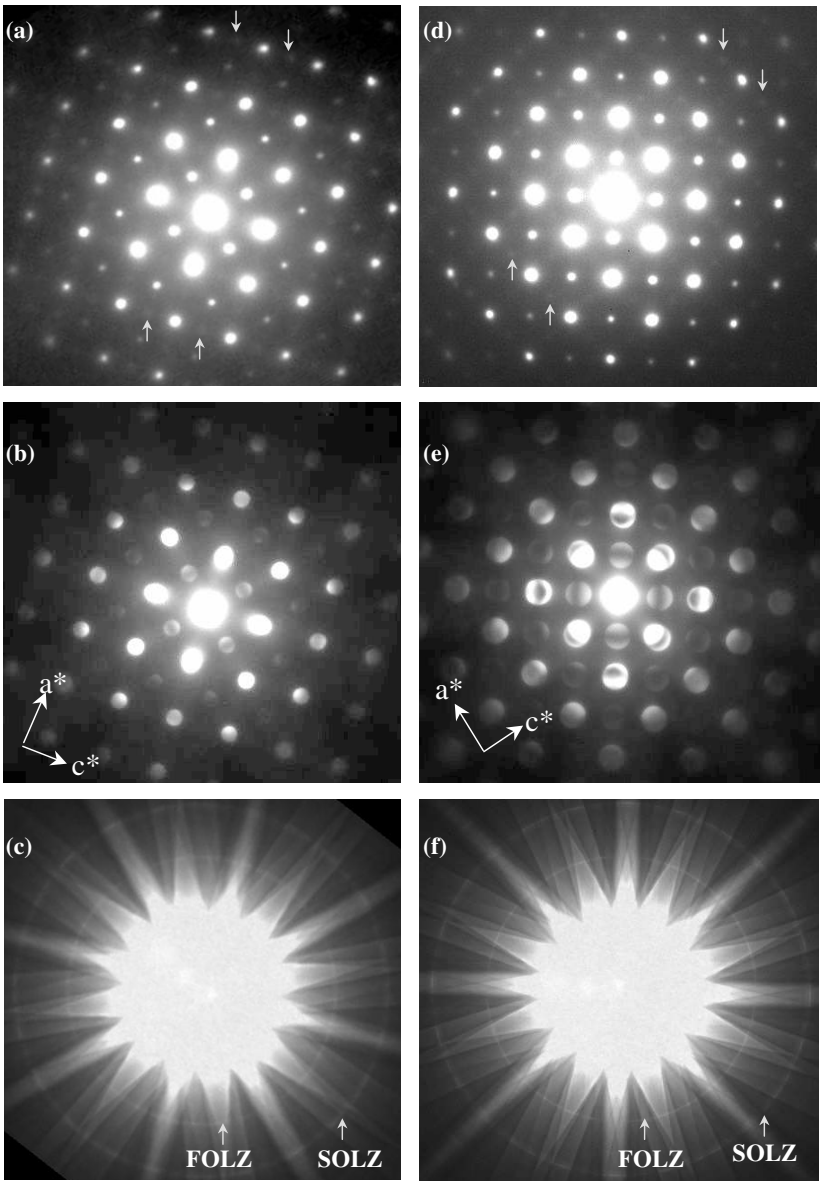

Figure 6. ((a), (d)) Selected area electron diffraction, ((b), (e)) low-angle CBED, and ((c), (f)) wide-angle CBED patterns from SCT20 ((a)–(c)) and SCT27 ((d)–(f)), respectively. These patterns have been taken along the [010] zone of the $Pnma$ phase. The axes indicated represent the directions a^* and c^* of the reciprocal lattice.

Figures 9 and 10 represent simulated zone patterns corresponding to [010]/[001] and [111] zones respectively for the above-mentioned space groups. For the calculation of these zone patterns we used only the lattice parameters and the extinction conditions of the space group used. Thus the circles in a simulated zone patterns simply represent the positions of the kinematically allowed reflections. It should be noted that in the [010] zone ZOLZ pattern of $P2_1/m$, all the reflections are allowed. If double diffraction is taken into account, which is

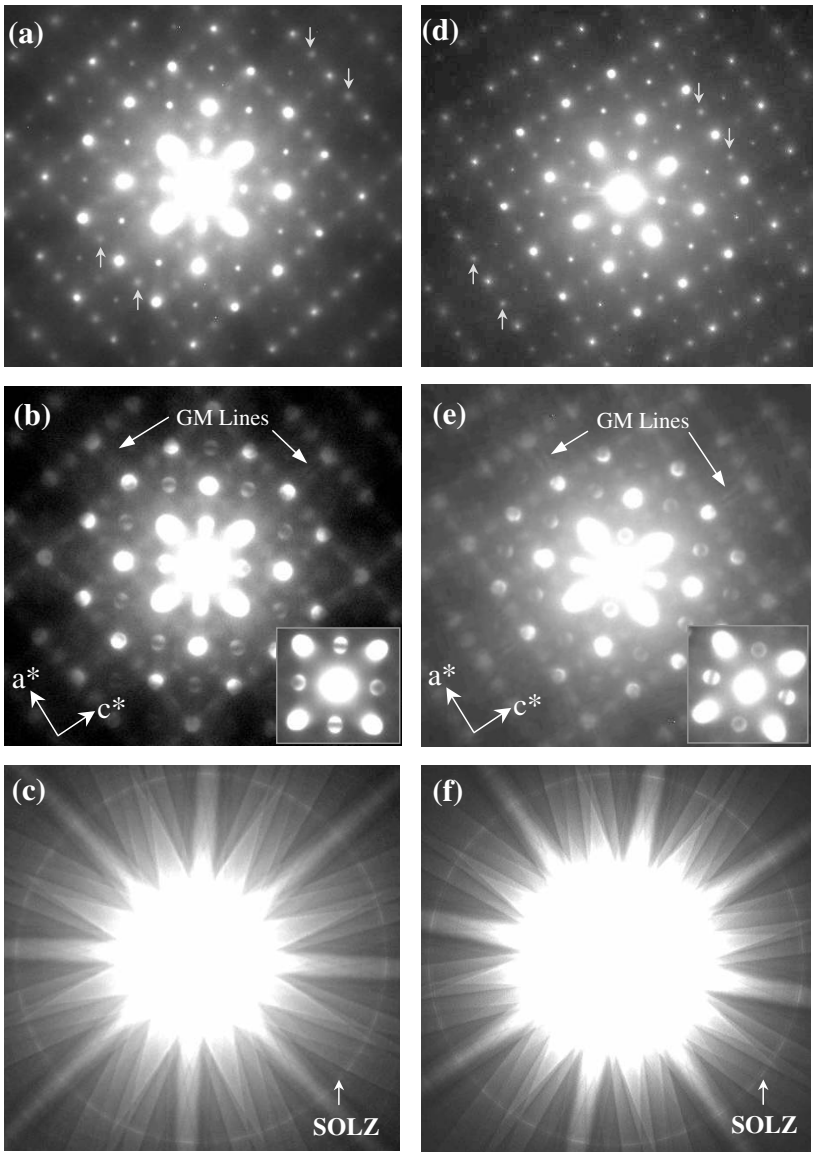

Figure 7. ((a), (d)) Zone-axis selected area electron diffraction, ((b), (e)) low-angle CBED, and ((c), (f)) wide-angle CBED patterns from SCT20 ((a)–(c)) and SCT27 ((d)–(f)), respectively. These patterns are identical to those shown in figure 5 corresponding to SCT30. The presence of mutually perpendicular GM-lines has been indicated by arrows. The insets in (b) and (e) show the unmodified central part of the corresponding CBED pattern.

quite likely to happen in the case of electron diffraction, the simulated patterns corresponding to [010] of $Pnma$ will look qualitatively similar to that of $P2_1/m$. But in the case of [010] of $Imma$ and [001] of $I4/mcm$, the double diffraction would in no way introduce any extra spot, and therefore they will never look, even qualitatively, similar to that of $Pnma$ or $P2_1/m$. Similarly, all the [111]-type zones of these space groups will look qualitatively similar if double diffraction is effectively operative.

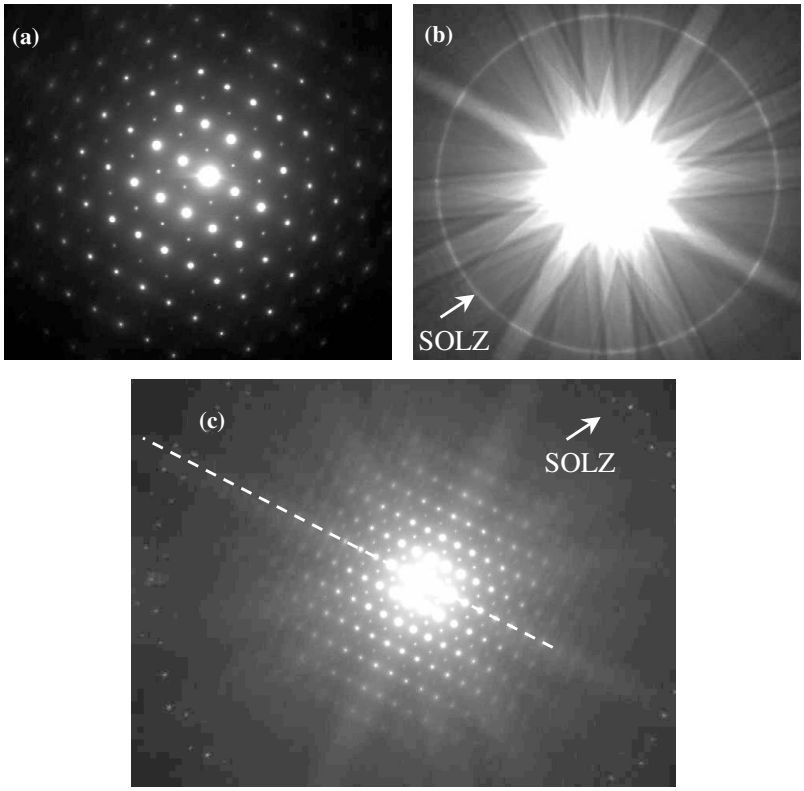

Figure 8. (a) Selected area electron diffraction pattern, (b) wide-angle CBED, and (c) focused micro-diffraction pattern along a [111]-type zone of SCT30.

The SAD patterns shown in figures 3(a), 5(a), 6(a), (d) and 7(a), (d), were carefully measured and found to correspond to a^*c^* reciprocal plane of the known (Ranjan and Pandey 2001b, Mishra *et al* 2002) orthorhombic cell. The HOLZ rings observed in patterns of figures 3(d), 5(d), 6(c), (f) and 7(c), (f), were found to correspond to FOLZ and SOLZ of the known orthorhombic cell. Thus the patterns shown in figures 3(a), 5(a), 6(a), (d) and 7(a), (d), correspond to the [010] zone only. It should be noted that the intensities of the superlattice spots in figures 5(a), 7(a) and (d) are higher compared to those in figures 3(a), 6(a) and (d), but the intensities of the corresponding FOLZ rings are otherwise. As is obvious from the simulated ZOLZ patterns, as shown in figures 9(d)–(f), double diffraction will in no way produce spots at positions matching the observed weak superlattice spots. Thus the occurrence of superlattice spots indicates that the observed patterns do not correspond to any structure having body-centered or face-centered lattices, and hence the possibilities of space groups $Imma$ and $I4/mcm$ are completely discarded. Tilting about a^* and c^* axes showed that the superlattice reflections with indices of $\{h00\}$ and $\{00l\}$ type (for odd values of h and l) become weaken and finally vanish; see figures 11(a) and (b). This indicates that these reflections are kinematically forbidden and have appeared only as a result of double diffraction.

The symmetry of the CBED patterns in figures 3(b) and 6(b), (e) is $2mm$, the mirrors being parallel to a^*b^* and c^*b^*. The symmetry of the bright-field (BF), that is the symmetry in the (000) disk, was also determined to be $2mm$. The BF mirrors are coincident with the dark-field (DF) mirrors. The presence of two mirrors in BF were realized only in the CBED patterns

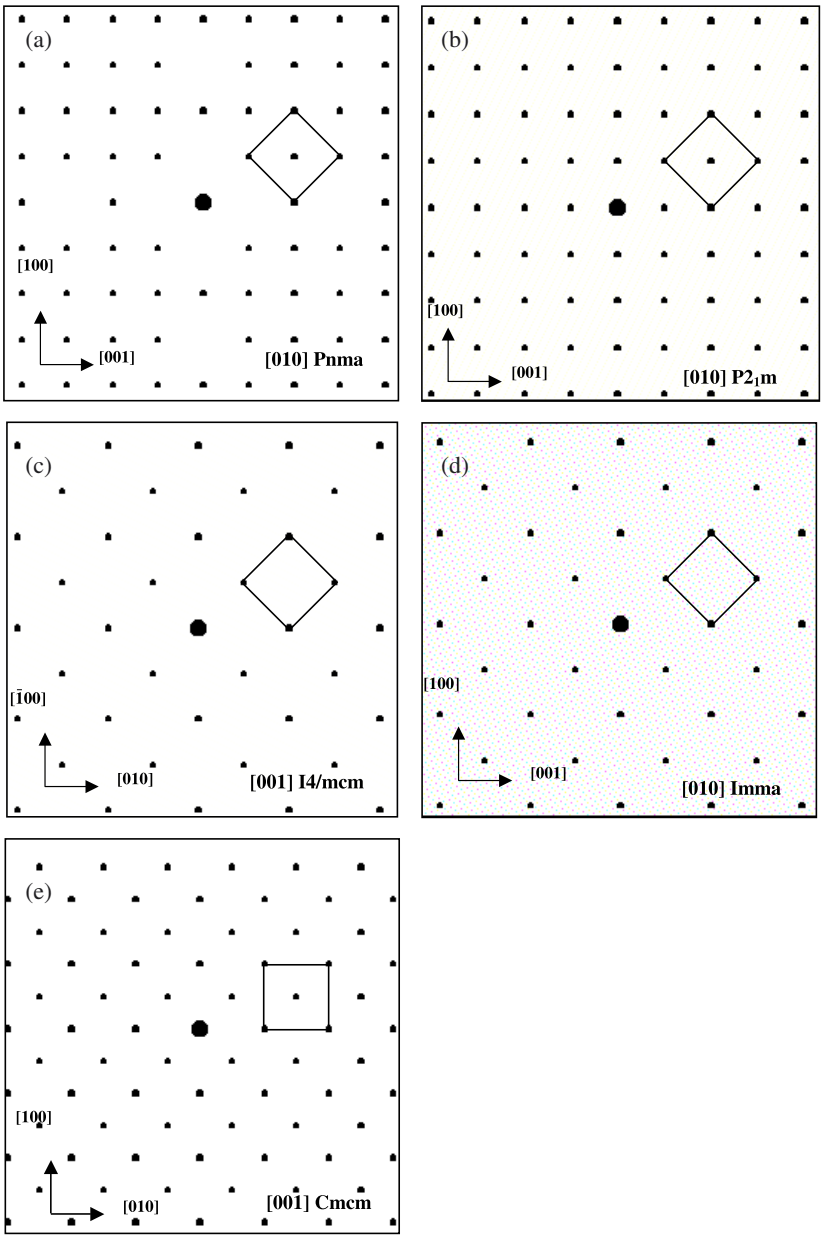

Figure 9. Simulated ZOLZ patterns along the long axis: (a) [010] of $Pnma$, (b) [010] of $P2_1/m$, (c) [001] of $Cmcm$, (d) [010] of $Imma$, and (e) [001] of $I4/mcm$. It should be noticed that after double diffraction the simulated patterns in (a)–(c) will look identical but no change will occur in the patterns (d) and (e).

obtained along directions tilted about the a^* and c^* axes, independently; see figures 12(a) and (b). The one taken exactly along [010] was not meaningful because of overlap of the disks due to the large lattice parameters in this case. Tilting about the a^* (or c^*) axis reduces the number of reflections around the BF disk (000), and hence the confusion due to disk overlaps

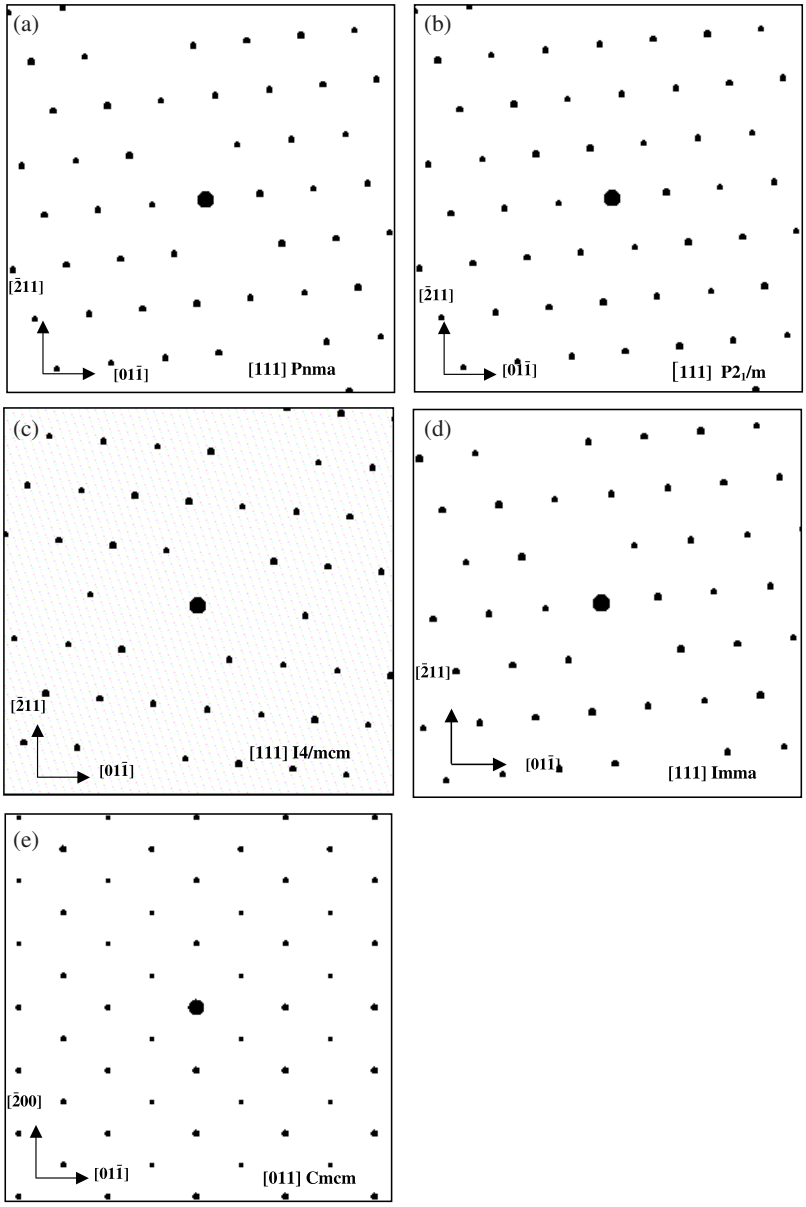

Figure 10. Simulated ZOLZ pattern along the [111] zone of (a) *Pnma*, (b) $P2_1/m$, (d) *Imma*, and (e) $I4/mcm$; and (c) along [011] of *Cmcm*.

minimizes. But in such unconventional settings, one will at some time get the information of one mirror only which will be perpendicular to the axis about which the tilt is performed. The presence of A_2-type GM-lines, although weak, can be seen in the kinematically forbidden reflections (500) and (005) in the modified CBED pattern; see figure 3(c). The presence of mutually perpendicular A_2-type GM-lines parallel to the mirrors, set in 2*mm* symmetry, reveals (Williams and Carter 1996) the presence of two mutually perpendicular glide planes containing the [010] axis. The presence of mutually perpendicular glide planes passing through [010]

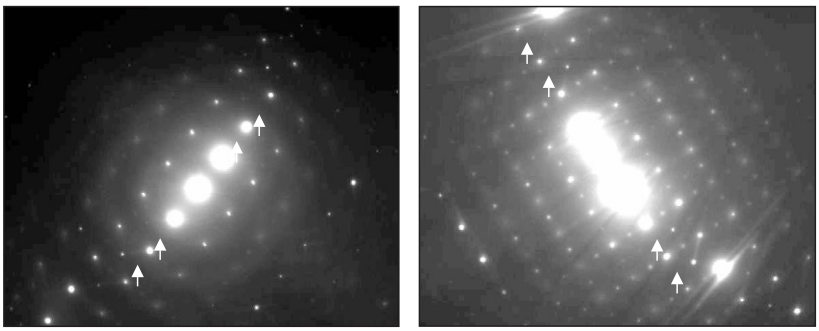

Figure 11. [010] Zone-axis SAD pattern tilted about a^* and c^*. It should be noted that $\{h00\}$-type and {00l}-type spots, as indicated by arrows, become extinct after tilting. This indicates that they appear due only to double diffraction.

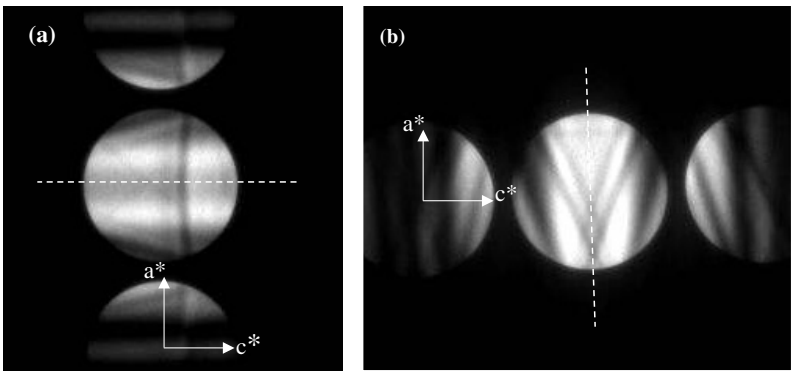

Figure 12. Wide-angle CBED disks showing mirrors perpendicular to (a) a^* and (b) c^*. This indicates the presence of $2mm$ bright-field (BF) symmetry in the [000] disk.

removes the possibility of $P2_1/m$ and $Cmcm$. The presence of $2mm$ both in the whole-pattern (WP) symmetry and BF symmetry indicates that the diffraction group is $2mm$ or $2mm1_R$, and hence the possible point groups for an orthorhombic cell are $mm2$ and mmm (Williams and Carter 1996, Steeds and Vincent 1983). Under the point group mmm the possible space group from the above-mentioned space groups with two mutually perpendicular glide planes converges to $Pnma$ ($Pbnm$) (International Tables for Crystallography 1992).

The presence of mutually perpendicular GM-lines along a^* and c^* in the CBED patterns can be clearly seen in figures 5(b) and 7(b), (e). The symmetry of the CBED pattern is only *two-fold*. Unlike the CBED shown in figure 3(b), there are no mirrors parallel to a^*b^* and c^*b^* planes. The BF symmetry was determined to be $2mm$. The mirrors are perpendicular to a^* and c^*. The method followed for this was the same as described above, and the BF disks obtained were similar, as shown in figures 12(a) and (b). The presence of mutually perpendicular A_2-type GM-lines can be seen in the kinematically forbidden reflections (300), (500), (003) and (005) in the pattern shown in figures 5(b) and 7(b), (e). The presence of mutually perpendicular A_2-type GM-lines not having any DF mirror but each perpendicular to BF mirrors set in $2mm$ symmetry reveals the presence of two mutually perpendicular screw axes normal to the [010] axis (Gjønnes and Moodie 1965, Williams and Carter 1996, Tanaka 1989). The presence of *two-fold* WP symmetry and $2mm$ BF symmetry indicates that the

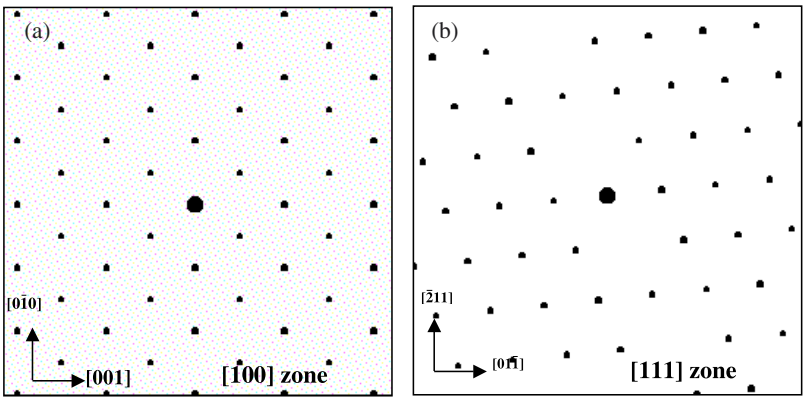

Figure 13. Simulated ZOLZ patterns along (a) the [100] zone and (b) the [111] zone of the *Pnma* phase. It should be noted that they would look identical in experimental patterns in which double diffraction may not be avoided.

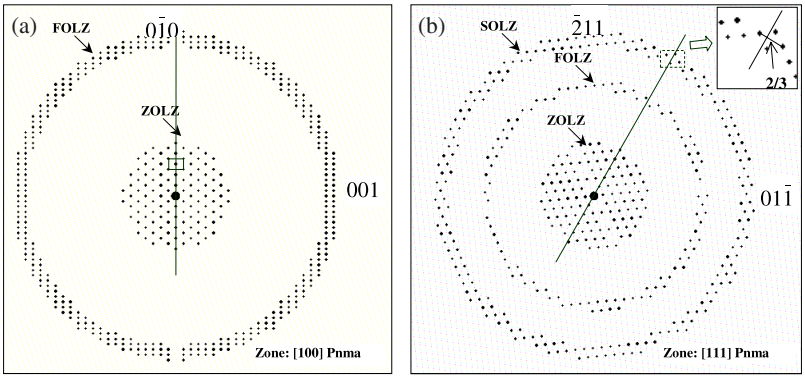

Figure 14. Simulated ZOLZ and HOLZ patterns of *Pnma* along (a) the [100] zone and (b) the [111] zone. The two zones can be identified by the relative shifts of HOLZ reflections with respect to the ZOLZ net, as indicated.

diffraction symmetry is $2m_R m_R$, and the only possible point group is 222 (Williams and Carter 1996, Steeds and Vincent 1983). Under the point group 222 the possible space groups with two mutually perpendicular screw axes converge to $P2_12_12$ (space group 18) and $P2_12_12_1$ (space group 19) (International Tables for Crystallography 1992).

The [111] zone SAD patterns, as shown in figure 6(a), recorded from regions R_1 and R_2 were found to be qualitatively the same. The absence of FOLZ rings was common to both regions. It is also imperative to describe at this juncture that the ZOLZ and wide-angle CBED patterns taken along [111]-type and [100]-type zones of *Pnma* look qualitatively similar; see the simulated ZOLZ and FOLZ patterns in figures 13(a) and (b). Therefore they need to be distinguished properly. One way to distinguish them is that [111] zone is tilted by 45° whereas [100] is at 90° from the unique zone [010]. The other way is to look into the micro-diffraction along these zones (Morniroli and Steeds 1992). The difference appears in the relative shift of the HOLZ reflections with respect to the ZOLZ net; see figures 14(a) and (b). The relative shift for [111] is 1/3 (or 2/3) along [1$\bar{2}$1] and that for [100] is 1/2 along [001]. The absence of the expected FOLZ ring appears to be due to two reasons: the presence of disorder and very weak scattered amplitude for the corresponding reflections of the FOLZ layer. In the presence of

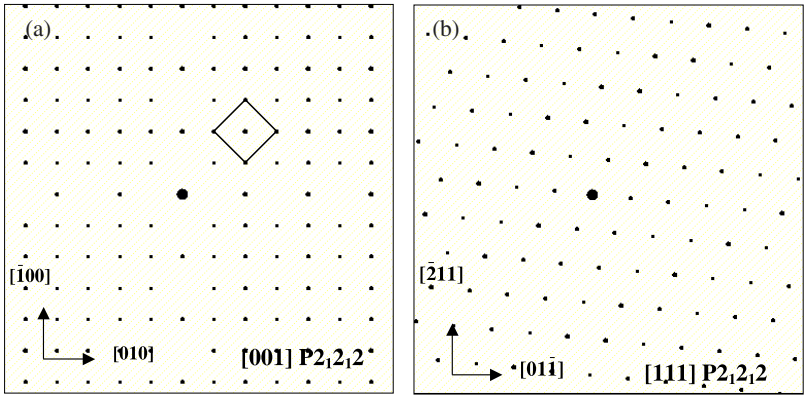

Figure 15. Simulated zone-axis diffraction patterns for (a) [100] and (b) [111] corresponding to $P2_12_12$ space group.

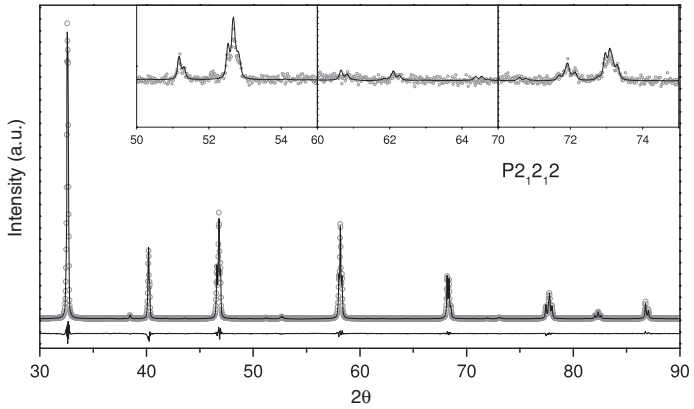

Figure 16. Rietveld refinement of XRD data of SCT30, with $P2_12_12$ phase ($\chi^2 = 3.59$). The data are the same as shown in figure 2. The inset shows enlarged views of the quality of fit for a few of the important superlattice peaks.

disorder the FOLZ reflections, which have ∼20 times large scattering vectors than the ZOLZ ones, will suffer a large phase change of $\sim 2\pi \cdot \mathrm{Exp}(g \cdot \Delta r)$ in its scattered amplitude and in the case of already low amplitude this may become too smeared out to be visible above the background. Here g and Δr are the scattering vector and the shift in atomic positions due to disorder.

Out of the two possibilities, $P2_12_12$ and $P2_12_12_1$, the correct choice was finalized by actually making the atomic structure of these phases containing the quadruple of basic perovskite structure. We could obtain success only for $P2_12_12$ and not for the $P2_12_12_1$. Hence the space group of the observed new phase is $P2_12_12$. For this space group the unique axis will be [001]. The ZOLZ simulations corresponding to [001] and [111] zones for $P2_12_12$ are shown in figures 15(a) and (b). It should be noted that the [001] zone of $P2_12_12$ looks identical to the simulated patterns for the [010] zone of $Pnma$, as shown in figure 9(a).

We fitted the XRD data using Rietveld refinement based on $P2_12_12$; see figure 16 (SCT30) and the corresponding inset. This shows a reasonably good fit, with a χ^2 value of 3.954. A better fit with improved χ^2 (2.72) is obtained by two-phase refinement of the data based on

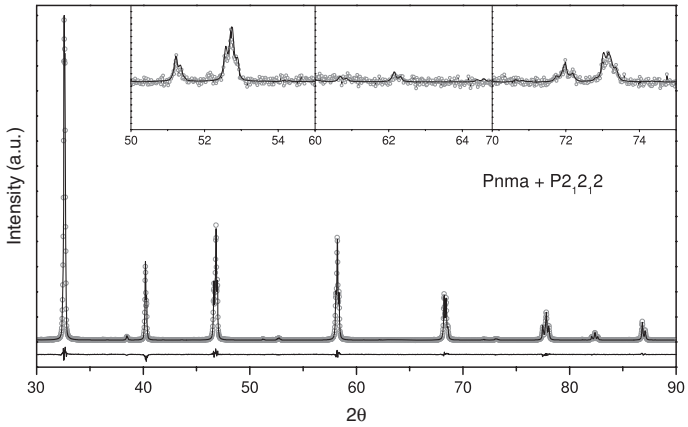

Figure 17. Rietveld refinement of XRD data of SCT30, based on two-phase refinement with $P2_12_12$ and *Pnma* phases. This fitting has an improved χ^2 value (2.72). The inset shows enlarged views of a few important superlattice peaks.

Table 1. The crystallographic parameters of the $P2_12_12$ phase obtained after two-phase refinement. The parameters for the *Pnma* phase were taken from Ranjan and Pandey (2001b).

			Positional coordinates		
Space group	Wyckoff position	Atoms	*X*	*Y*	*Z*
$P2_12_12$	2(b)	Sr/Ca	0	0.5	0.252 84
	2(b)	Sr/Ca	0	0.5	0.752 73
	2(a)	Ti	0	0	0.002 37
	2(a)	Ti	0	0	0.499 82
	2(a)	O1	0	0	0.789 22
	2(a)	O2	0	0	0.264 25
	4(c)	O3	0.171 18	0.298 97	0.476 49
	4(c)	O4	0.265 49	0.239 01	0.005 57
	$a = 5.4818(2)$		$b = 5.4844(2)$		$c = 7.7878(3)$

Pnma and $P2_12_12$; see figure 17 (SCT30) and the corresponding inset. From the two-phase fit we could estimate the volume fractions of *Pnma* and $P2_12_12$ to be about 40% and 60%, respectively. This matches quite satisfactorily with the frequent observation of the $P2_12_12$ phase during TEM explorations. The refined Wyckoff positions and the lattice parameters of $P2_12_12$ phase are given in table 1.

The observed new phase with space group $P2_12_12$ does not appear in the list of space groups suggested by Glazer (1972), (1975) based on the analysis of the effect of pure 3D tilt of the BO_6 octahedra with respect to its orientation in the basic perovskite structure with space group $Pm3m$. This newly observed phase appears to be a result of the mixed effect of rotation as well as translation of the oxygen sublattice resulting effectively as a distortion of the oxygen octahedra.

4. Conclusion

Based on the above-described results of powder x-ray diffraction and TEM analysis of $Sr_{1-x}Ca_xTiO_3$ for $x = 0.20, 0.27$ and 0.30, we conclude that an orthorhombic phase with space group $P2_12_12$ coexists with the already known *Pnma* phase. The presence of this new phase

$P2_12_12$ has been confirmed through a TEM analysis including ZOLZ, HOLZ simulations of the observed SAD patterns, a symmetry analysis including GM-lines in CBED patterns, and the Rietveld refinement of room-temperature XRD data corresponding to the studied compositions. Unlike in earlier reports, we had observed the occurrence of both $P2_12_12$ and $Pnma$ phases. The volume fraction of the two phases was determined to be about 60% & 40% respectively, by two-phase Rietveld refinement of the XRD data for all three samples. To the best of our knowledge no such result about the identification of the new orthorhombic phase with space group $P2_12_12$ has been reported yet.

Acknowledgments

The authors gratefully acknowledge Dr P Chaddah, the Director, and Professor Ajay Gupta, the Center Director, of UGC-DAE CSR-Indore for their encouragement and interest in the work. We also gratefully acknowledge the fruitful discussions with Professor O N Siravastava, Department of Physics, BHU-Varanasi. One of the authors (SA) would also like to acknowledge CSIR-India for financial support as an SRF.

References

Ball C J, Begg B D, Cookson D J, Thorogood G J and Vance E R 1998 *J. Solid State Chem.* **139** 238–47
Bernorz J G and Muller K A 1984 *Phys. Rev. Lett.* **52** 2289
Carpenter M A, Howard C J, Knight K S and Zhang Z 2006 *J. Phys.: Condens. Matter* **18** 10725
Ceh M, Krasevec V and Kolar D 1987 *J. Solid State Chem.* **68** 68
Cowley R A 1980 *Adv. Phys.* **29** 1
Gjønnes J and Moodie A F 1965 *Acta Crystallogr.* **19** 65–7
Glazer A M 1972 *Acta Crystallogr.* B **28** 3384
Glazer A M 1975 *Acta Crystallogr.* A **31** 756
Granicher H and Jakits O 1954 *Nuovo Cimento* **9** (suppl.) 480
Hembergger J, Luckenheimer P, Viana R, Bohmer R and Loidl A 1995 *Phys. Rev.* B **52** 3159
Howard C J, Withers R L and Kennedy B J 2001 *J. Solid State Chem.* **160** 8–12
Howard C J, Withers R L, Zhang Z, Osaka K, Kato K and Takata M 2005 *J. Phys.: Condens. Matter* **17** L459
International Tables for Crystallography 1992 vol A Kluwer–Academic
Jaffe B, Cook W R and Jaffe H 1971 *Piezoelectric Ceramics* (London: Academic)
Mishra S K, Ranjan R and Pandey D 2002 *J. Appl. Phys.* **91** 4447
Mitsui T and Westphal W B 1961 *Phys. Rev.* B **124** 1354
Qin S, Becarro A I, Seifert F, Gottsmaun J and Jiang J 2000 *J. Mater. Chem.* **10** 1609
Ranjan R, Pandey D and Lalla N P 2000 *Phys. Rev. Lett.* **84** 3726
Ranjan R and Pandey D 2001a *J. Phys.: Condens. Matter* **13** 4239–49
Ranjan R and Pandey D 2001b *J. Phys.: Condens. Matter* **13** 4251–66
Ranjan R, Pandey D, Schuddinck W, Richard O, Meulencere P D, Landuyt J V and Tandeloo G V 2001 *J. Solid State Chem.* **162** 20–8
Ranson P, Ouillon R, Pinan-Lucarre J P, Pruzan Ph, Mishra S K, Ranjan R and Pandey D 2005 *J. Raman Spectrosc.* **36** 898–911
Steeds J W and Vincent R 1983 *J. Appl. Crystallogr.* **16** 317–24
Woodward D I, Wise P L, Lee W E and Reaney I M 2006 *J. Phys.: Condens. Matter* **18** 2401
Morniroli J P and Steeds J W 1992 *Ultramicroscopy* **45** 219
Tanaka M 1989 *J. Electron Microsc. Tech.* **13** 27–39
Uwe H and Sakudo T 1976 *Phys. Rev.* B **13** 271
Williams D B and Carter C B 1996 *Transmission Electron Microscopy-Diffraction II* (New York: Platinum Press)